Inorg. Chem. **2008**, *47*, 9569−9582

Molecular Wheels: New Mn_{12} Complexes as Single-Molecule Magnets

Sonali J. Shah,[†] Christopher M. Ramsey,[‡] Katie J. Heroux,[†] Antonio G. DiPasquale,[†] Naresh S. Dalal,[§] Arnold L. Rheingold,[†] Enrique del Barco,*[,‡] and David N. Hendrickson*[,†]

Department of Chemistry and Biochemistry, University of California at San Diego, La Jolla, California 92093, Department of Physics, University of Central Florida, Orlando, Florida 32765, and Department of Chemistry, Florida State University, Tallahassee, Florida 32306

Received July 22, 2008

The preparation, structure and magnetic properties of three new wheel-shaped dodecanuclear manganese complexes, $[Mn_{12}(Adea)_8(CH_3COO)_{14}]\cdot 7CH_3CN$ (**1**$\cdot 7CH_3CN$), $[Mn_{12}(Edea)_8(CH_3CH_2COO)_{14}]$ (**2**) and $[Mn_{12}(Edea)_8(CH_3COO)_2(CH_3CH_2COO)_{12}]$ (**3**), are reported, where $Adea^{2-}$ and $Edea^{2-}$ are dianions of the *N*-allyl diethanolamine and the *N*-ethyl diethanolamine ligands, respectively. Each complex has six Mn(II) and six Mn(III) ions alternating in a wheel-shaped topology, with eight *n*-substituted diethanolamine dianions. All variable-temperature direct current (DC) magnetic susceptibility data were collected in 1, 0.1, or 0.01 T fields and in the 1.8−300 K temperature range. Heat capacity data, collected in applied fields of 0−9 T and in the 1.8−100 K temperature range, indicate the absence of a phase-transition due to long-range magnetic ordering for **1** and **3**. Variable-temperature, variable-field DC magnetic susceptibility data were obtained in the 1.8−10 K and 0.1−5 T ranges. All complexes show out-of-phase signals in the AC susceptibility measurements, collected in a 50−997 Hz frequency range and in a 1.8−4.6 K temperature range. Extrapolation to 0 K of the in-phase AC susceptibility data collected at 50 Hz indicates an $S = 7$ ground state for **1**, **2**, and **3**. Magnetization hysteresis data were collected on a single crystal of **1** in the 0.27−0.9 K range and on single crystals of **2** and **3** in the 0.1−0.9 K temperature range. Discrete steps in the magnetization curves associated with resonant quantum tunneling of magnetization (QTM) confirm these complexes to be single-molecule magnets. The appearance of extra QTM resonances on the magnetic hysteresis of **1** is a result of a weak coupling between two Mn ions at opposite ends of the wheel, dividing the molecule into two ferromagnetic exchange-coupled $S = {}^7/_2$ halves. The absence of these features on **2** and **3**, which behave as rigid spin $S = 7$ units, is a consequence of different interatomic distances.

Introduction

Single-molecule magnets (SMMs) have been of considerable interest to scientists ever since their initial discovery in 1993.[1] SMMs are transition metal complexes that have a large spin ground state and considerable negative magnetoanisotropy leading to a barrier for the reversal of magnetization. These molecules show slow magnetization relaxation and can be magnetized below their blocking temperature.[2] The first SMM to be discovered was $[Mn_{12}O_{12}(CH_3COO)_{16}(H_2O)_4]\cdot 2CH_3COOH\cdot 4H_2O$, a dodecanuclear manganese cluster with an $S = 10$ ground state that is commonly known as Mn_{12}-Ac.[1] This complex shows magnetization hysteresis and also shows quantum tunneling of the magnetization as evidenced by steps at regular intervals in the hysteresis loop.[2]

Since the discovery of Mn_{12}-Ac, a large number of new SMMs have been reported with a wide variety of topologies, nuclearities, and metal atoms including Mn, Ni, and Fe. However, manganese clusters exhibiting SMM behavior remain the most abundant. Many derivatives of Mn_{12}-Ac have been reported to show SMM behavior such as

* To whom correspondence should be addressed. E-mail: dhendrickson@ucsd.edu (D.N.H), delbarco@physics.ucf.edu (E.d.B.).
[†] University of California at San Diego.
[‡] University of Central Florida.
[§] Florida State University.

(1) (a) Sessoli, R.; Tsai, H.-L.; Schake, A. R.; Wang, S.; Vincent, J. B.; Folting, K.; Gatteschi, D.; Christou, G.; Hendrickson, D. *J. Am. Chem. Soc.* **1993**, *115*, 1804. (b) Sessoli, R.; Gatteschi, D.; Caneschi, A.; Novak, M. A. *Nature* **1993**, *365*, 141.

(2) (a) Gatteschi, D.; Sessoli, R. *Angew. Chem., Int. Ed.* **2003**, *42*, 269. (b) Friedman, J. R.; Sarachik, M. P.; Tejada, J.; Maciejewski, J.; Ziolo, R. *J. Appl. Phys.* **1996**, *79*, 6031.

10.1021/ic801374u CCC: $40.75
Published on Web 09/26/2008

$[Mn_{12}O_{12}(O_2CCH_2Bu^t)_{16}(H_2O)_4]$[3] and the mixed-carboxylate complex $[Mn_{12}O_{12}(O_2CCHCl_2)_8(O_2CCH_2Bu^t)_8(H_2O)_3]$, which was reported[4] to have an $S = 10$ ground state. The complex $[Mn_{12}O_{12}(O_2CC_6H_4\text{-}2\text{-}CH_3)_{16}(H_2O)_4]\cdot CH_2Cl_2\cdot 2H_2O$, reported by Rumberger et al.,[5] is also a SMM and shows Jahn−Teller isomerism. The most extensively studied Fe SMM is $[Fe_8O_2(OH)_{12}(tacn)_6]Br_8$, where tacn is triazocyclononane, which has an $S = 10$ ground state.[6]

SMMs incorporating other transition metals such as cobalt or vanadium are relatively rare. An example of a cobalt SMM is the $[Co_4(hmp)_4(MeOH)_4Cl_4]$ complex, which has four Co(II) ions, which was reported by Yang et al. and shows magnetization hysteresis at low temperatures.[7] The hmp^- ligand is a chelating ligand in this complex, where hmp^- is the anion of 2-hydroxymethylpyridine. A SMM of vanadium has also been reported with the formula $[V_4O_2(O_2CPh)_7(bpy)_2]ClO_4$, where bpy is 2,2′-bipyridine, and an $S = 3$ ground state.[8]

Some of the different topologies seen in Mn SMMs include the Mn_4 dicubane[9] complexes and the $S = {}^9/_2$ Mn_4 cubane[10] complexes. Other interesting topologies include rod-shaped SMMs such as the Mn_6 clusters[11] and one-dimensional chains of weakly interacting SMMs such as $[Mn_4(hmp)_6Cl_2]_n(ClO_4)_{2n}$, reported by Yoo et al.[12] However, perhaps the most interesting of these topologies is that of the wheel-shaped SMMs which have fascinated scientists in multiple disciplines for a number of reasons.[13] For example, odd-numbered molecular wheels, such as $[(C_6H_{11})_2NH_2][Cr_8NiF_9(O_2CC(CH_3)_3)_{18}]$, are of interest for studying spin frustration.[14] It is also believed that molecular wheels could be used to study important features of quantum computing.[15] Furthermore, antiferromagnetic molecular wheels show quantum tunneling of the Néel vector which is not normally observed in extended antiferromagnets since the lowest lying excitations are spin waves. In antiferromagnetic wheels, however, the lowest lying excitations correspond to rotation of the Néel vector.[16] Quantum tunneling of the Néel vector was also observed by inelastic neutron scattering experiments for the $CsFe_8$ antiferromagnetic molecular wheel with the formula $[Cr_8F_8\{O_2CC(CH_3)_3\}_{16}]\cdot 0.25C_6H_{14}$.[17]

This family of wheel-shaped complexes that show SMM behavior is steadily growing. One of the smallest of these molecular wheels is the recently reported tetranuclear manganese complex, $[Mn_4(anca)_4(Htea)_2(dbm)_2]\cdot 2.5Et_2O$, reported by Beedle et al.[18] Larger wheels include the $[Mn_{24}]$ wheel,[19] the $[Mn_{22}]$ wheels,[20] and the $[Mn_{84}]$ wheel,[21] which is the largest wheel-shaped SMM known to date. The largest reported spin ground state for a wheel-shaped SMM is $S = 14$ for the $[Mn_{16}O_2(OCH_3)_{12}(tmp)_8(CH_3COO)_{10}]\cdot 3Et_2O$ wheel reported by Manoli et al. in 2007.[22]

A smaller subgroup of the wheel-shaped SMMs is the family of single-stranded wheels including the series of $[Mn_{16}]$ wheels, which are the largest single-stranded loops known to date.[23] The extensively studied $[Ni_{12}]$ wheel is also a member of this family and has an $S = 12$ ground state resulting from a ferromagnetic exchange interaction between pairs of nickel ions.[24] A series of $[Mn_{12}]$ wheels reported by Rumberger et al.[25] in 2005 are also examples of single-stranded wheels. Three complexes were reported: $[Mn_{12}(Bdea)_8(CH_3COO)_{14}]\cdot 3CH_3CN$, $[Mn_{12}(Edea)_8(CH_3COO)_{14}]$, and $[Mn_{12}(Mdea)_8(CH_3COO)_4]$,[25] where $Bdea^{2-}$ is the dianion of *N*-butyl diethanolamine, $Edea^{2-}$ is the dianion of *N*-ethyl diethanolamine, and $Mdea^{2-}$ is the dianion of *N*-methyl diethanolamine. The wheel complex $[Mn_{12}(Mdea)_8(CH_3COO)_4]$ was first communicated in 2004[26] and shows an out-of-phase signal in the AC susceptibility, characteristic of SMM behavior.

We herein report three new $[Mn_{12}]$ wheel-shaped single-molecule magnets. These complexes are structural analogs of the $[Mn_{12}]$ wheels previously reported by Rumberger et al.[25] Two of these complexes were synthesized using simple

(3) Soler, M.; Wernsdorfer, W.; Sun, Z.; Ruiz, D.; Huffman, J. C.; Hendrickson, D. N.; Christou, G. *Polyhedron* **2003**, *22*, 1783.
(4) Soler, M.; Artus, P.; Folting, K.; Huffman, J. C.; Hendrickson, D. N.; Chrsitou, G. *Inorg. Chem.* **2001**, *40*, 4902.
(5) Rumberger, E. M.; del Barco, E.; Lawrence, J.; Hill, S.; Kent, A. D.; Zakharov, L. N.; Rheingold, A. L.; Hendrickson, D. N. *Polyhedron* **2005**, *24*, 2557.
(6) (a) Sangregorio, C.; Ohm, T.; Paulsen, C.; Sessoli, R.; Gatteschi, D. *Phys. Rev. Lett.* **1997**, *78*, 4645. (b) Delfs, C.; Gatteschi, D.; Pardi, L.; Sessoli, R.; Wieghardt, K.; Hanke, D. *Inorg. Chem.* **1993**, *32*, 3099. (c) Wieghardt, K.; Pohl, K.; Jibril, I.; Huttner, G. *Angew. Chem., Int. Ed.* **1984**, *23*, 77.
(7) Yang, E.-C.; Hendrickson, D. N.; Wernsdorfer, W.; Nakano, M.; Zakharov, L. N.; Sommer, R. D.; Rheingold, A. L.; Gairaud, M.; Christou, G. *J. Appl. Phys.* **2002**, *91*, 7382.
(8) Castro, S. L.; Sun, Z.; Grant, C. M.; Bollinger, J. C.; Hendrickson, D. N.; Christou, G. *J. Am. Chem. Soc.* **1998**, *120*, 2365.
(9) Yoo, J.; Yamaguchi, A.; Nakano, M.; Krzystek, J.; Streib, W. E.; Brunel, L.; Ishimoto, H.; Christou, G.; Hendrickson, D. N. *Inorg. Chem.* **2001**, *40*, 4604.
(10) Aubin, S. M. J.; Wemple, M. W.; Adams, D. M.; Tsai, H.-L.; Christou, G.; Hendrickson, D. N. *J. Am. Chem. Soc.* **1996**, *118*, 7746.
(11) Milios, C. J.; Manoli, M.; Rajaraman, G.; Mishra, A.; Budd, L.; White, F.; Parsons, S.; Wernsdorfer, W.; Christou, G.; Brechin, E. *Inorg. Chem.* **2006**, *45*, 6782.
(12) Yoo, J.; Wernsdorfer, W.; Yang, E. C.; Nakano, M.; Rheingold, A. L.; Hendrickson, D. N. *Inorg. Chem.* **2005**, *44*, 3377.
(13) Hoffmann, R. *Sci. Am.* **1993**, *268*, 66.
(14) Cador, O.; Gatteschi, D.; Sessoli, R.; Larsen, F. K.; Overgaard, J.; Barra, A. L.; Teat, S. J.; Timco, G. A.; Winpenny, R. E. P. *Angew. Chem., Int. Ed.* **2004**, *43*, 5196.
(15) Affronte, M.; Casson, I.; Evangilisti, M.; Candini, A.; Carreta, S.; Muryn, C. A.; Teat, S. J.; Timco, G. A.; Wernosdorfer, W.; Winpenny, R. E. P. *Angew. Chem., Int. Ed.* **2005**, *44*, 6496.
(16) Waldmann, O.; Dobe, C.; Mutka, H.; Furrer, A.; Gudel, H. U. *Phys. Rev. Lett.* **2005**, *95*, 057202.
(17) Waldmann, O. *Coord. Chem. Rev.* **2005**, *249*, 2550.
(18) Beedle, C. C.; Heroux, K. J.; Nakano, M.; DiPasquale, A.; Rheingold, A.; Hendrickson, D. N. *Polyhedron* **2007**, *26*, 2200.
(19) Scott, R.; Milios, C.; Vinslava, A.; Lifford, D.; Parsons, S.; Wernsdorfer, W.; Christou, G.; Brechin, E. *Dalton Trans.* **2006**, 3161.
(20) Murugesu, M.; Raftery, J.; Wernsdorfer, W.; Christou, G.; Brechin, E. K. *Inorg. Chem.* **2004**, *43*, 4203.
(21) Tasiopolous, A.; Vinslava, A.; Wernsdorfer, W.; Abboud, K.; Christou, G. *Angew. Chem., Int. Ed.* **2004**, *43*, 2117.
(22) Manoli, M.; Prescimone, A.; Mishra, A.; Parsons, S.; Christou, G.; Brechin, E. K. *Dalton Trans.* **2007**, 532.
(23) (a) Murugesu, M.; Wernsdorfer, W.; Abboud, K.; Christou, G. *Angew. Chem., Int. Ed.* **2005**, *44*, 892. (b) Shah, S. J.; Ramsey, C. M.; Heroux, K. J.; O'Brien, J. R.; DiPasquale, A. G.; Rheingold, A. L.; del Barco, E.; Hendrickson, D. N. *Inorg. Chem.* **2008**, *47*, 6245.
(24) (a) Cadiou, C.; Murrie, M.; Paulsen, C.; Villar, V.; Wernsdorfer, W.; Winpenny, R. E. P. *Chem. Commun.* **2001**, 2666. (b) Andres, H.; Basler, R.; Blake, A. J.; Cadiou, C.; Chaboussant, G.; Grant, C. M.; Gudel, H.; Murrie, M.; Parsons, S.; Paulsen, C.; Semadini, F.; Villar, V.; Wernsdorfer, W.; Winpenny, R. E. P. *Chem.—Eur. J.* **2002**, *8*, 4867.
(25) Rumberger, E. M.; Shah, S. J.; Beedle, C. C.; Zakharov, L. N.; Rheingold, A. L.; Hendrickson, D. N. *Inorg. Chem.* **2005**, *44*, 2742.
(26) Rumberger, E. M.; Zakharov, L. N.; Rheingold, A. L.; Hendrickson, D. N. *Inorg. Chem.* **2004**, *43*, 6531.

Mn(II) salts with N-substituted diethanolamine ligands. The third complex was synthesized using an N-substituted diethanolamine ligand and $[Mn_{12}O_{12}(CH_3CH_2COO)_{16}(H_2O)_3]$ as the starting material. Magnetization versus magnetic field hysteresis data were collected for single crystals of these three new $[Mn_{12}]$ wheel-shaped complexes. Steps are seen in the hysteresis loops for all three complexes indicative of quantum tunneling of the magnetization. However, unusual observations in the magnetic data of one of these complexes will be further analyzed and discussed.

Experimental Section

All manipulations were performed under aerobic conditions. The chemicals Mn(II)acetate, *N*-ethyl diethanolamine, *N*-allyl diethanolamine, and triethylamine were purchased from Sigma-Aldrich. Mn(II)propionate and $[Mn_{12}O_{12}(CH_3CH_2COO)_{16}(H_2O)_3]$ were prepared as described.[27,28]

$[Mn_{12}(Adea)_8(CH_3COO)_{14}]\cdot 7CH_3CN$ (1·7CH$_3$CN). To Mn(II)acetate (1.22 g, 5 mmol) in 75 mL of dichloromethane was added 1 equiv of the ligand *N*-allyl diethanolamine (0.72 g, 5 mmol) in 25 mL of dichloromethane. Addition of 1 equiv of triethylamine (0.69 mL, 5 mmol) resulted in a deep reddish-brown solution that was stirred overnight. A white precipitate was obtained that was filtered off. A subsequent evaporation of the filtrate by vacuum distillation yielded a brown oil to which was added 100 mL of acetonitrile. Plate-shaped crystals of **1** were formed after approximately 1 week by slow evaporation of the acetonitrile solution. The overall yield was 18%. Selected IR data (KBr, cm^{-1}): 3500 (m, br), 2900 (m), 1600 (s), 1400 (s), 1100 (s), 700 (m). Anal. Calcd (found) for $C_{84}H_{146}Mn_{12}N_8O_{44}$: C, 38.34 (38.18); H, 5.59 (5.28); N, 4.25 (4.28).

$[Mn_{12}(Edea)_8(CH_3CH_2COO)_{14}]$ (2). To a solution of $[Mn_{12}O_{12}(CH_3CH_2COO)_{16}(H_2O)_3]$ (0.5 g, 0.25 mmol) in 50 mL of dichloromethane was added 8 equiv of the ligand *N*-ethyl diethanolamine (0.266 g, 2 mmol) in 25 mL dichloromethane. After the solution was stirred for 2 days, it was filtered. The solution was then evaporated by vacuum distillation to yield an oil to which was added 80 mL of acetonitrile. Crystals of **2** were obtained in the flask after allowing the acetonitrile solution to sit at room temperature for 2 days. The yield was 43%. Selected IR data (KBr, cm^{-1}): 3500 (m, br), 2900 (m), 1600 (s), 1400 (s), 1100 (s), 600 (m). Anal. Calcd (found) for $C_{90}H_{174}Mn_{12}N_8O_{44}$: C, 39.57 (39.33); H, 6.42 (6.04); N, 4.1 (4.28).

$[Mn_{12}(Edea)_8(CH_3COO)_2(CH_3CH_2COO)_{12}]$ (3). To a 75 mL dichloromethane solution of Mn(II)acetate (0.61 g, 2.5 mmol) and Mn(II)propionate (0.51 g, 2.5 mmol) was added 1 equiv of the ligand *N*-ethyldiethanolamine (0.665 g, 2.5 mmol) in 25 mL of dichloromethane. Addition of 2 equiv of triethylamine (0.69 mL, 5 mmol) after a few minutes resulted in a brown solution that was stirred overnight. The solution was then evaporated by vacuum distillation to yield an oil to which was added 80 mL of acetonitrile. The solution was allowed to sit at room temperature for 2 days after which brown crystals of **3** were obtained. The yield was 21%. Selected IR data (KBr, cm^{-1}): 3500 (m, br), 2900 (m), 1600 (s), 1400 (s), 1100 (m), 600 (m). Anal. Calcd (found) for $C_{83.58}H_{156.74}Mn_{12}N_8O_{44}$: C, 39.09 (38.32); H, 6.33 (5.89); N, 4.14 (4.59).

Physical Measurements. Infrared spectra were recorded using KBr discs on a Thermo-Nicolet Avatar series spectrometer. All elemental analyses were performed by NuMega Resonance Labs (San Diego, CA). The dc magnetic susceptibility data were collected using a Quantum Design MPMS SQUID magnetometer equipped with a 5 T magnet at the University of California at San Diego. Microcrystalline samples were restrained using eicosane to prevent torquing. Diamagnetic corrections were applied using Pascal's constants to the magnetic susceptibility data. The ac magnetic susceptibility data were collected on a Quantum Design MPMS SQUID magnetometer equipped with a 1 T magnet also at the University of California at San Diego. Magnetization hysteresis measurements were carried out on single crystals of complexes **1**, **2**, and **3** using a micro-Hall effect magnetometer[29] at the University of Central Florida. Hysteresis measurements were carried out at temperatures as low as 0.27 K in an Oxford Instruments ^{3}He cryostat. Heat capacity data were collected at Florida State University using a Quantum Design Physical Property Measurement System (PPMS). Heat capacity data were collected using a sample size of 1 mg. A small amount of apiezon N grease was used to attach the sample to a thermally conducting platform. Heat capacity data were collected employing a measurement technique reported by Bachmann et al.,[30] reviewed by Stewart,[31] and summarized by Cage et al.[32]

X-ray Crystallography. Crystals were mounted on a CryoLoop with Paratone-N oil. Diffraction intensity data were collected at 100, 173, and 208 K (for **1**, **2**, and **3**, respectively) on a Bruker Smart Apex CCD diffractometer with Mo Kα radiation, integrated using the Bruker SAINT software program, and corrected for absorption using the Bruker SADABS program. Crystallographic data and refinement parameters for all three complexes are given in Table 1.

Complexes **1** and **2** were solved by direct methods (SHELXS-97), developed by successive difference Fourier syntheses, and refined by full-matrix least-squares on all F^2 data. All non-hydrogen atoms were refined anisotropically by full-matrix least-squares (SHELXL-97). All hydrogen atoms were placed using a riding model. In complex **1**, one acetonitrile solvate molecule was modeled, while the remaining disordered solvate molecules were treated by the Squeeze method, the details of which can be found in the CIF file. There were no cocrystallized solvate molecules in **2**. The C34 and C35 atoms of the $Adea^{2-}$ ligand in **1**, as well as the C3 and C15 atoms of the ethyl acetate ligands in **2**, are positionally disordered yielding larger than normal thermal ellipsoids.

For complex **3**, solution by Patterson methods (DIRDIF-99) produced a complete heavy-atom phasing model consistent with the proposed structure. All non-hydrogen atoms were refined anisotropically by full-matrix least-squares (SHELXL-97). All hydrogen atoms were placed using a riding model with their positions constrained relative to their parent atom using the appropriate HFIX command in SHELXL-97. The carbon atoms of the $Edea^{2-}$ ligand (C37 and C38) are also positionally disordered as in **1**. Acetate/propionate disorder is observed throughout the molecule resulting in partial occupancy of atoms C3, C6, C9, C12, C15, and C20, the details of which can be found in the CIF file.

(27) Guillem, A.; Bhaduri, S.; Artus, P.; Huffman, J.; Hendrickson, D. N.; Christou, G. *Polyhedron* **2002**, *21*, 1779.
(28) Eppley, H.; Tsai, H-L; de Vries, N.; Folting, K.; Christou, G.; Hendrickson, D. N. *J. Am. Chem. Soc.* **1995**, *117*, 301.
(29) Kent, A. D.; von Molnar, S.; Gider, S.; Awschalom, D. D. *J. Appl. Phys.* **1994**, *76*, 6656.
(30) Bachmann, R.; DiSalvo, F. J.; Geballe, T. J.; Greene, R. L.; Howard, R. E.; King, C. N.; Kirsch, H.C/; Schwall, R. E.; Thomas, H. U.; Zubeck, R. B. *Rev. Sci. Instrum.* **1972**, *43*, 205.
(31) Stewart, G. R. *Rev. Sci. Instrum.* **1983**, *54*, 1.
(32) Cage, B.; Dalal, N. S. *Chem. Mater.* **2001**, *13*, 880.

Table 1. Crystallographic Data and Refinement Parameters for **1**, **2**, and **3**

	1	2	3
formula	$C_{84}H_{146}Mn_{12}N_8O_4 \cdot 7(CH_3CN)$	$C_{90}H_{174}Mn_{12}N_8O_{44}$	$C_{83.58}H_{156.74}Mn_{12}N_8O_{44}$
formula weight	2713.48	2731.65	2637.16
temp [K]	100(2)	173(2)	208(2)
wavelength [Å]	0.71073	0.71073	0.71073
crystal system	triclinic	monoclinic	monoclinic
space group	$P\bar{1}$	$P2_1/n$	$P2_1/n$
a [Å]	16.0122(11)	11.1757(11)	11.146(2)
b [Å]	16.3029(11)	17.0725(16)	17.113(3)
c [Å]	16.5860(11)	32.207(3)	32.331(6)
α [deg]	63.1040(10)	90	90
β [deg]	66.1200(10)	98.3020(10)	97.215(4)
γ [deg]	61.0910(10)	90	90
V [Å^3]	3282.7(4)	6080.6(10)	6118.0(19)
Z	1	2	2
cryst color, habit	brown plate	brown blade	brown blade
D_{calcd} (mg m^{-3})	1.373	1.492	1.431
abs coeff [mm^{-1}]	1.187	1.282	1.271
F(000)	1509	2844	2732.4
cryst size [mm^3]	0.30 × 0.15 × 0.10	0.40 × 0.08 × 0.04	0.20 × 0.10 × 0.07
θ range	1.42−27.53°	1.35−26.00°	2.19−25.03°
comp to θ [25.00°]	95.0%	99.8%	99.9%
max/min transm	0.8905 and 0.7171	0.950 and 0.884	0.9163 and 0.7851
refinement method		full-matrix least-squares on F^2	
data/restraints/params	14382/0/708	11918/0/705	10811/0/702
GOF on F^2	0.993	1.026	1.276
R1 ($I > 2\sigma(I)$)[a,b]	0.0416	0.0415	0.0978
R1 (all data)[a,b]	0.0595	0.0604	0.1147
largest diff peak/hole, e·Å^{-3}	0.797/−0.461	0.905/−0.706	0.893/−0.659

[a] $R = \sum||F_o| - |F_c||/\sum|F_o|$. [b] $R(\omega F^2) = \{\sum[\omega(F_o^2 - F_c^2)^2]/\sum[\omega(F_o^2)^2]\}^{1/2}$; $\omega = 1/[\sigma^2(F_o^2) + (aP)^2 + bP]$; $P = [2F_c^2 + \max(F_o,0)]/3$.

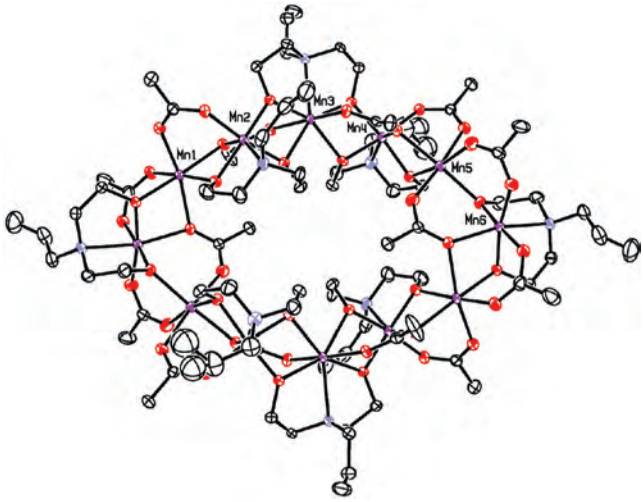

Figure 1. ORTEP of $[Mn_{12}(Adea)_8(CH_3COO)_{14}] \cdot 7CH_3CN$ (**1**·7CH$_3$CN). Hydrogen atoms have been omitted for clarity. Thermal ellipsoids at 50% probability level.

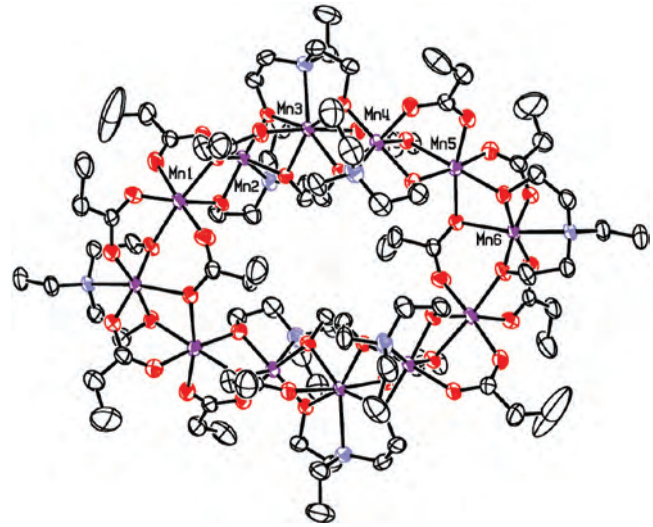

Figure 2. ORTEP of $[Mn_{12}(Edea)_8(CH_3CH_2COO)_{14}]$ (**2**). Hydrogen atoms have been omitted for clarity. Thermal ellipsoids at 50% probability level.

Results and Discussion

Crystal Structures. ORTEP diagrams of **1**, **2**, and **3** are shown in Figures 1, 2, and 3, respectively. Selected bond distances and angles for all three complexes are shown in Tables 2 and 3. Each complex comprises a $[Mn_{12}]$ wheel, which is structurally analogous to the series of $[Mn_{12}]$ wheel complexes reported by Rumberger et al.[25] in 2005. These wheels consist of six Mn(II) and six Mn(III) ions arranged in an alternating, single-stranded wheel topology. Adea^{2-} and Edea^{2-} are the *N*-allyldiethanolamine and the *N*-ethyldiethanolamine ligands, respectively. The oxidation states of the Mn atoms were determined by charge considerations, the presence of Jahn−Teller distortion around the high-spin Mn(III) atoms, and bond valence sum analyses.

$[Mn_{12}(Adea)_8(CH_3COO)_{14}] \cdot 7CH_3CN$ (1·7CH$_3$CN). Complex **1** crystallized in the triclinic $P\bar{1}$ space group; an ORTEP of the wheel-shaped structure is shown in Figure 1. The asymmetric unit consists of one-half of the target molecule with the equivalent atom positions generated by the symmetry transformation $-x + 1, -y + 1, -z + 1$. There is only one orientation of the wheel within the unit cell. Each molecule has six Mn(II) and six Mn(III) ions alternating in a single-stranded wheel topology bridged by eight Adea^{2-} ligands as well as 14 bridging acetates. The Mn(III) ions (Mn2, Mn4, Mn6, and their symmetry-equivalent atoms)

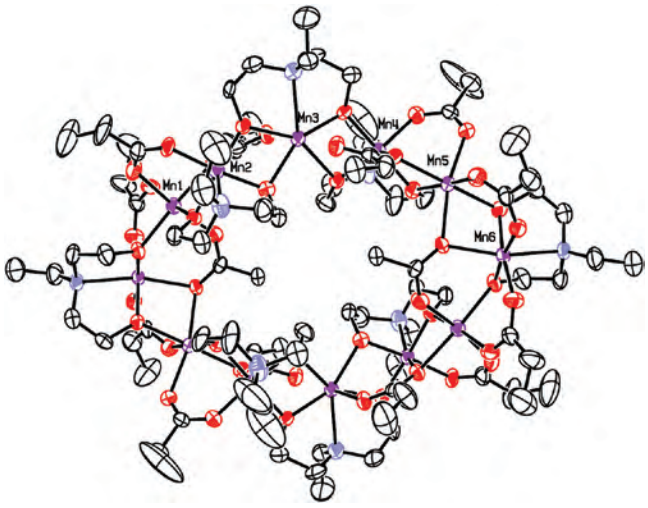

Figure 3. ORTEP for $[Mn_{12}(Edea)_8(CH_3COO)_2(CH_3CH_2COO)_{12}]$ (**3**). Hydrogen atoms have been omitted for clarity. Thermal ellipsoids at 50% probability level.

Table 2. Selected Interatomic Distances [Å] for **1**, **2**, and **3**

	1·7CH_3CN	**2**	**3**
Mn(1)−O(1)	2.1600(19)	2.195(2)	2.2259(10)
Mn(1)−O(3)	2.2121(17)	2.218(2)	2.2151(9)
Mn(1)−O(12)	2.2410(18)	2.137(2)	2.1499(9)
Mn(1)−O(14)	2.1445(19)	2.158(2)	2.1739(11)
Mn(1)−O(15)	2.1094(18)	2.157(2)	2.1520(10)
Mn(1)−O(22)	2.1839(17)	2.145(2)	2.1337(10)
Mn(2)−O(2)	1.9703(18)	1.964(2)	1.9638(9)
Mn(2)−O(3)	2.2468(19)	2.207(2)	2.2268(9)
Mn(2)−O(15)	1.9232(17)	1.921(2)	1.9175(9)
Mn(2)−O(16)	1.8929(17)	1.891(2)	1.8970(10)
Mn(2)−O(17)	1.8775(17)	1.886(2)	1.8889(10)
Mn(2)−N(1)	2.362(2)	2.393(3)	2.3802(12)
Mn(3)−O(4)	2.2291(18)	2.252(2)	2.2295(10)
Mn(3)−O(5)	2.2064(18)	2.270(2)	2.2420(10)
Mn(3)−O(16)	2.2582(17)	2.191(2)	2.1888(10)
Mn(3)−O(17)	2.2065(18)	2.263(2)	2.2595(10)
Mn(3)−O(18)	2.2731(17)	2.219(2)	2.2034(10)
Mn(3)−O(19)	2.1955(18)	2.243(2)	2.2628(9)
Mn(3)−N(2)	2.439(2)	2.428(3)	2.4380(13)
Mn(4)−O(6)	2.2088(18)	2.204(2)	2.2410(10)
Mn(4)−O(7)	1.9570(17)	1.961(2)	1.9608(10)
Mn(4)−O(18)	1.8913(17)	1.880(2)	1.8845(9)
Mn(4)−O(19)	1.8916(17)	1.895(2)	1.8970(10)
Mn(4)−O(20)	1.9298(17)	1.930(2)	1.9291(10)
Mn(4)−N(3)	2.357(2)	2.371(3)	2.3564(14)
Mn(5)−O(6)	2.1825(17)	2.222(2)	2.2281(9)
Mn(5)−O(8)	2.1946(18)	2.177(2)	2.1828(11)
Mn(5)−O(9)	2.175(2)	2.127(2)	2.1378(12)
Mn(5)−O(11)	2.1407(19)	2.230(2)	2.2440(10)
Mn(5)−O(20)	2.1770(18)	2.113(2)	2.1139(10)
Mn(5)−O(21)	2.1373(17)	2.178(2)	2.1898(9)
Mn(6)−O(10)	1.9329(18)	1.972(2)	1.9780(9)
Mn(6)−O(12)	2.2031(17)		
Mn(6)−O(11)		2.207(2)	2.2074(9)
Mn(6)−O(13)	1.9735(18)	1.937(2)	1.9391(9)
Mn(6)−O(21)	1.8973(18)	1.912(2)	1.8978(9)
Mn(6)−O(22)	1.9014(18)	1.895(2)	1.9019(9)
Mn(6)−N(4)	2.379(2)	2.350(2)	2.3557(11)

exhibit six-coordinate, distorted octahedral geometry with average JT-distorted Mn(III)−O bonds of 2.22 Å and Mn(III)−N bonds of 2.37 Å. The Jahn−Teller elongation axes of Mn2, Mn4, and their symmetry-related atoms are nearly parallel to one another and orthogonal to the average plane of the wheel (as shown in Figure S1, Supporting Information). The remaining two Jahn−Teller elongation axes of Mn6 and its symmetry-equivalent atom are oriented orthogonal to the other JT axes and are thus virtually in plane with the $[Mn_{12}]$ ring. This arrangement of the Mn(III) distortion is nearly identical to that found in the previously reported $[Mn_{12}]$ wheels.[25]

Table 3. Selected Bond Angles [deg] for **1**, **2**, and **3**

	1·7CH_3CN	**2**	**3**
O(15)−Mn(1)−O(14)	170.95(7)	173.77(9)	170.04(4)
O(15)−Mn(1)−O(3)	76.49(7)	77.24(8)	77.36(3)
O(15)−Mn(1)−O(1)	91.33(7)	84.19(9)	82.96(4)
O(15)−Mn(1)−O(22)	98.36(7)	94.64(8)	96.97(4)
O(14)−Mn(1)−O(1)	96.44(7)	89.60(10)	87.75(4)
O(14)−Mn(1)−O(22)	86.57(7)	86.62(9)	87.43(4)
O(14)−Mn(1)−O(3)	99.38(7)	101.66(9)	98.32(4)
O(1)−Mn(1)−O(22)	87.98(7)	96.27(9)	95.21(4)
O(17)−Mn(2)−O(16)	83.74(7)	82.03(9)	82.01(4)
O(16)−Mn(2)−O(15)	95.93(7)	94.27(9)	94.29(4)
O(16)−Mn(2)−O(2)	171.53(8)	173.35(9)	173.36(4)
O(17)−Mn(2)−O(3)	96.30(7)	97.38(10)	97.38(4)
O(17)−Mn(2)−O(15)	175.74(8)	176.30(9)	176.25(4)
O(17)−Mn(2)−O(2)	89.35(8)	91.58(9)	91.93(4)
O(15)−Mn(2)−O(2)	91.32(8)	92.11(9)	91.80(4)
O(19)−Mn(3)−O(5)	88.56(7)	80.67(8)	82.24(4)
O(19)−Mn(3)−O(4)	94.39(7)	92.32(8)	91.54(4)
O(5)−Mn(3)−O(4)	172.01(7)	172.98(9)	173.51(4)
O(19)−Mn(3)−O(17)	148.53(6)	149.47(8)	148.77(3)
O(17)−Mn(3)−O(5)	85.51(7)	99.15(8)	99.40(4)
O(17)−Mn(3)−O(4)	88.12(7)	86.72(9)	86.87(4)
O(19)−Mn(3)−O(16)	80.64(6)	81.89(7)	80.91(4)
O(18)−Mn(4)−O(19)	82.57(7)	82.91(9)	83.00(4)
O(19)−Mn(4)−O(20)	93.60(7)	96.54(9)	96.20(4)
O(19)−Mn(4)−O(7)	174.01(7)	171.35(10)	171.63(4)
O(18)−Mn(4)−O(6)	101.01(7)	99.00(9)	98.27(4)
O(20)−Mn(4)−O(6)	83.49(7)	79.41(9)	79.78(4)
O(18)−Mn(4)−O(20)	174.10(8)	178.33(10)	177.92(4)
O(18)−Mn(4)−O(7)	91.45(7)	89.73(9)	89.71(4)
O(20)−Mn(4)−O(7)	92.39(7)	90.94(9)	91.22(4)
O(19)−Mn(4)−O(6)	90.90(7)	90.00(8)	89.38(4)
O(7)−Mn(4)−O(6)	89.89(7)	95.65(9)	95.76(4)
O(21)−Mn(5)−O(11)	91.40(7)	74.90(8)	75.17(3)
O(11)−Mn(5)−O(9)	92.60(8)	87.09(9)	87.44(4)
O(11)−Mn(5)−O(20)	96.66(7)	93.70(8)	91.17(4)
O(21)−Mn(5)−O(6)	176.87(7)	177.25(8)	177.10(3)
O(21)−Mn(5)−O(9)	87.81(7)	86.45(9)	87.04(4)
O(21)−Mn(5)−O(20)	99.55(7)	102.25(8)	101.19(4)
O(9)−Mn(5)−O(20)	168.00(7)	171.17(9)	171.02(4)
O(11)−Mn(5)−O(6)	86.27(7)	106.37(8)	106.26(3)
O(21)−Mn(6)−O(22)	92.39(8)	93.33(10)	92.92(4)
O(22)−Mn(6)−O(10)	169.49(8)	173.44(9)	174.00(4)
O(22)−Mn(6)−O(13)	90.01(8)	93.09(10)	93.39(4)
O(21)−Mn(6)−O(10)	93.67(8)	89.78(9)	90.27(4)
O(21)−Mn(6)−O(13)	176.21(8)	170.87(9)	171.53(4)
O(10)−Mn(6)−O(13)	83.52(8)	83.20(9)	82.96(4)
O(21)−Mn(6)−O(12)	94.78(7)		
O(21)−Mn(6)−O(11)		80.85(8)	82.05(4)
O(10)−Mn(6)−O(12)	103.66(7)		
O(10)−Mn(6)−O(11)		92.42(9)	91.66(4)
O(22)−Mn(6)−O(12)	84.36(7)		
O(22)−Mn(6)−O(11)		93.78(9)	93.81(4)

Each Mn(III) ion is chelated by an $Adea^{2-}$ ligand in a tridentate fashion with the amine nitrogen and the two deprotonated alcohol arms bound to the metal. The two alkoxide oxygen atoms bound to the Mn(III) ions also bridge the adjacent Mn(II) ions on either side. The two remaining $Adea^{2-}$ ligands are bound to seven-coordinate, distorted pentagonal bipyramidal Mn(II) ions (Mn3 and its symmetry-equivalent atom). All other Mn(II) ions (Mn1, Mn5, and their symmetry-equivalent atoms) exhibit six-coordinate, distorted octahedral geometry bound only to acetate or alkoxide oxygen atoms.

The acetate ligands in this structure adopt two different binding modes. Eight of the acetate ligands form an η^1,η^1,μ_2 bridge between each Mn(III) ion and adjacent six-coordinate Mn(II) ion. Four of the acetate ligands adopt the η^1,η^2,μ_3 bridging mode between each seven-coordinate Mn(II) ion, adjacent Mn(III) ion, and six-coordinate Mn(II) ion. The remaining two acetate ligands also bind in the η^1,η^2,μ_3 mode but form a bridge linking the six-coordinate Mn(II) ion, the adjacent Mn(III) ion, and another six-coordinate Mn(II) ion. The η^1,η^2,μ_3-acetate ligands all point toward the interior of the wheel whereas the η^1,η^1,μ_2-acetates are located on the periphery of the wheel. Analogous bonding was also seen in the previously reported [Mn_{12}] wheels.[25]

Of special relevance, in regards to the magnetic results reported in the following sections, is the distance between the Mn5 and Mn6 ions ($d_{56} \approx 3.489$ Å), which is larger than the distance separating the rest of the Mn ions within the wheel (average distance $d_{avg} = 3.173$ Å), giving a ratio of $R = d_{56}/d_{avg} = 1.0995$.

The unit cell of **1** contains a single orientation of the [Mn_{12}] wheel that exhibits C_i site symmetry. A stereo packing diagram of **1** can be found in Figure S3, Supporting Information. The wheels pack rather tightly in alternating layers with their easy axes (through the center of each ring) oriented parallel to one another. The easy axis is assumed to be perpendicular to the molecular plane (hard plane) of the wheel, which is taken as the average plane containing Mn2, Mn3, Mn4, and their symmetry-equivalent ions. This plane is rotated ~21° from the (100) Miller plane, or the *bc* plane, and ~48° from the (010) plane (*ac* plane) of the crystal. The distance between the layers formed by the wheels (measured between the average planes of the wheels) is 8.5 Å. One ordered acetonitrile solvate molecule is located above and below each wheel (related by a center of inversion). The electron density due to disordered solvate molecules, along with the modeled solvate molecules, occupies the voids between each layer but not the interior of the wheels. There are no H-bonding or appreciable van der Waals interactions (intra- or intermolecular) within the crystal lattice.

[Mn_{12}(Edea)$_8$(CH_3CH_2COO)$_{14}$] (2). Complex **2** crystallized in the monoclinic $P2_1/n$ space group; an ORTEP of the wheel-shaped structure is shown in Figure 2. The asymmetric unit consists of one-half of the target molecule with the equivalent atom positions generated by the symmetry transformation $-x, -y, -z$. Complex **2** exhibits the same [Mn_{12}] core as seen in the structure of **1**; however, all of the $Adea^{2-}$ and acetate ligands are occupied by $Edea^{2-}$ and propionate ligands, respectively.

The crystal structure of **2** is comparable to **1** in that it contains six Mn(II) (two seven-coordinate and four six-coordinate) and six Mn(III) ions in an alternating wheel arrangement. The average JT-distorted bond lengths are 2.21 Å for Mn(III)−O and 2.37 Å for Mn(III)−N. The Jahn−Teller axes are oriented in the same directions as in **1**, which can be seen in Figure S1, Supporting Information. All of the $Edea^{2-}$ ligands exhibit the same binding modes as in complex **1**. The propionates occupy nearly analogous positions as the acetate ligands in **1** where eight are in the η^1,η^1,μ_2 bridging mode and six are in the η^1,η^2,μ_3 bridging mode. There is a slight structural difference in the two μ_3-acetates bound to the Mn(III) ion and the two six-coordinate Mn(II) ions on either side in that the η^2 sight bridges Mn5 and Mn6 in **2** as opposed to bridging Mn1 and Mn6′ as seen in **1**. The distance between the Mn1 and Mn6′ ions in this wheel is $d_{16} \approx 3.496$ Å, also larger than the distance separating the rest of the Mn ions within the wheel, $d_{avg} = 3.1988$ Å), giving a ratio of $R = d_{16}/d_{avg} = 1.0929$, which is smaller than that in complex **1**.

The unit cell of **2** contains two different orientations of the [Mn_{12}] unit (Figure S2, Supporting Information), all related by inversion. The wheels pack along the *a*-axis of the unit cell in parallel stacks with neighboring wheels of the same orientation. Since there are two different orientations of the wheel, there are two sets of alternating stacks, which pack in a staggered formation throughout the lattice, eliminating any large voids. The molecular planes of both orientations of the wheel (defined as in complex **1**), and thus their perpendicular easy axes, form an angle of 48° ± 3° between them. There are no solvate molecules cocrystallized with the wheel and no appreciable intra- or intermolecular interactions. The closest intermolecular wheel−wheel distance is 3.57 Å between the ethyl arm of an $Edea^{2-}$ ligand and the alkoxide oxygen of an η^1,η^2,μ_3-propionate on an adjacent wheel.

[Mn_{12}(Edea)$_8$(CH_3COO)$_2$(CH_3CH_2COO)$_{12}$] (3). Complex **3** also crystallizes in the monoclinic $P2_1/n$ space group; an ORTEP of the wheel-shaped structure is shown in Figure 3. Complexes **2** and **3** have nearly identical unit cell parameters with **3** having a slightly smaller β-angle and larger volume. The asymmetric unit consists of one-half of the target molecule with the equivalent atom positions generated by the symmetry transformation $-x + 2, -y + 2, -z$. Complex **3** exhibits the same [Mn_{12}] core as seen in the structure of **2**; however, two of the propionate ligands are replaced by acetates.

The average Jahn−Teller distorted bond lengths are 2.23 Å for Mn(III)−O and 2.36 Å for Mn(III)−N. The direction of this disorder, in comparison to **1** and **2**, is illustrated in Figure S1, Supporting Information. The only structural difference between **2** and **3** is that the two propionates exhibiting the η^1,η^2,μ_3 binding mode between the Mn(III) ion and the two six-coordinate Mn(II) ions are replaced by two acetate ligands in **3**. These acetate ligands, however, exhibit the same bridging mode as the corresponding propionates in **2** with the η^2-sites bridging the Mn1 and Mn6′ ions. The distance between the Mn1 and Mn6′ ions in this wheel is $d_{16} \approx 3.488$ Å, while that between the rest of the ions is $d_{avg} = 3.1956$ Å, giving a ratio of $R = d_{16}/d_{avg} = 1.0915$, which is also smaller than that in complex **1** but comparable to that in complex **2**.

The crystal packing of **3** is nearly identical to that of **2**, *vide supra*. A stereo packing diagram of **3** can also be found in Figure S4, Supporting Information. The easy axes of the two wheels in the unit cell are separated by a larger angle of 58.5° ± 3° as opposed to the 48° observed in **2**. As in **2**, complex **3** is also free of solvate molecules and shows no

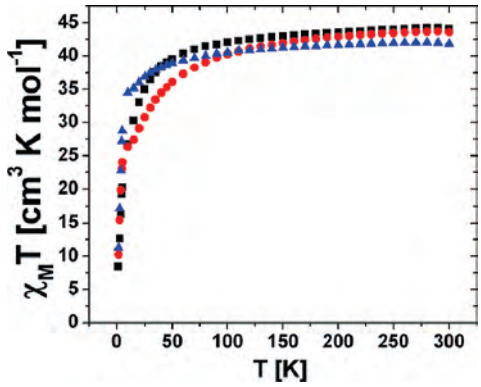

Figure 4. Plot of $\chi_M T$ versus temperature for $[Mn_{12}(Adea)_8(CH_3COO)_{14}]\cdot 7CH_3CN$ ($\mathbf{1}\cdot 7CH_3CN$) (●), $[Mn_{12}(Edea)_8(CH_3CH_2COO)_{14}]$ (**2**) (■) and $[Mn_{12}(Edea)_8(CH_3COO)_2(CH3CH2COO)_{12}]$ (**3**) (▲). The data were collected with an applied field of 1 T in the temperature range of 300−1.8 K.

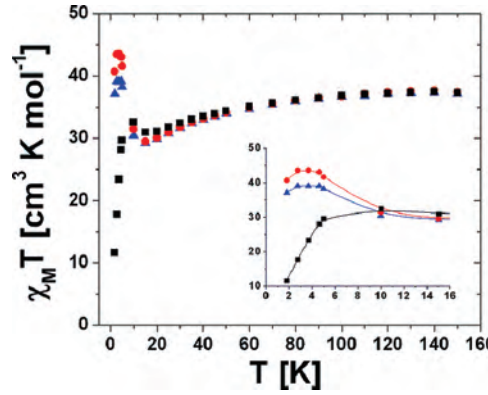

Figure 5. Field dependence for $[Mn_{12}(Adea)_8(CH_3COO)_{14}]\cdot 7CH_3CN$ ($\mathbf{1}\cdot 7CH_3CN$). Data were collected at applied fields of 1 (■), 0.1 (▲) and 0.01 T (●) and in the temperature range of 300−1.8 K.

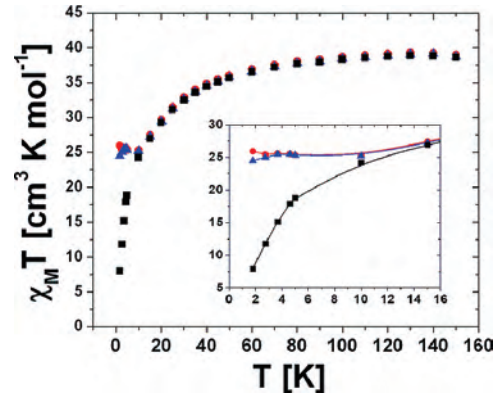

Figure 6. Field dependence for $[Mn_{12}(Edea)_8(CH_3CH_2COO)_{14}]$ (**2**). Data were collected at fields of 1 (■), 0.1 (▲), and 0.01 T (●) and in the temperature range of 1.8−300 K.

reasonably close intermolecular interactions. The closest intermolecular wheel−wheel interaction is 3.71 Å but is found between two alkyl groups, not involving any of the alkoxide oxygen bridges.

All three complexes appear to have weak Mn(II)−Mn(III) interactions at opposite ends of the wheel. Structurally, this is because the Mn1−Mn6′ interaction in complexes **2** and **3** (or Mn5−Mn6 in complex **1**) involves only one direct Mn−O−Mn bridge whereas the other Mn_2 pairs involve two direct oxide linkages. The angle of this single Mn−O−Mn bridge is also larger (∼119°) in complex **1** compared with the remaining Mn−O−Mn angles of 92−104° in the wheel. These values are comparable to those observed in the previously reported $[Mn_{12}]$ wheel $[Mn_{12}(Mdea)_8(CH_3COO)_{14}]\cdot CH_3CN$, where the Mn1−Mn6′ distance is ∼3.47 Å and the Mn1−O−Mn6′ angle is ∼117°.[25] A DFT study was performed on this wheel complex in order to determine the nature of its unusual spin ground state. It was proposed that the wheel might actually consist of two $S = {}^7/_2$ halves weakly coupled antiferromagnetically at the Mn1−Mn6 junctions leading to an overall $S = 7$ ground-state for the complete wheel. The magnetic exchange between Mn1 and Mn6 was calculated by DFT to be nearly 0 cm^{-1}, further supporting this hypothesis.[33]

DC Magnetic Susceptibility Studies. DC magnetic susceptibility data were recorded on microcrystalline samples of **1**, **2**, and **3** in the temperature range of 1.8−300 K in an applied field of 1 T. The DC magnetic susceptibility data for $[Mn_{12}(Adea)_8(CH_3COO)_{14}]\cdot 7CH_3CN$ ($\mathbf{1}\cdot 7CH_3CN$) are shown in Figure 4. The product of the molar magnetic susceptibility and the absolute temperature ($\chi_M T$) for **1** at 300 K is 43.6 cm^3·K·mol^{-1}. The $\chi_M T$ value gradually decreases with decreasing temperature until a value of 10.2 cm^3·K·mol^{-1} is reached at 1.8 K. The DC magnetic susceptibility data are plotted as $\chi_M T$ vs T for $[Mn_{12}(Edea)_8(CH_3CH_2COO)_{14}]$ (**2**) and are also shown in Figure 4. The value of $\chi_M T$ is 44.0 cm^3·K·mol^{-1} at 300 K and gradually decreases as the temperature is decreased until a value of 8.5 cm^3·K·mol^{-1} is reached at 1.8 K. The $\chi_M T$ vs T data for $[Mn_{12}(Edea)_8(CH_3COO)_2(CH_3CH_2COO)_{12}]$ (**3**) are shown in Figure 4. The $\chi_M T$ value for **3** at 300 K is 41.8 cm^3·K·mol^{-1} and remains more or less constant as the temperature is decreased to 100 K. Below 100 K, there is a slight decrease in the $\chi_M T$ value with a decrease in temperature until a value of 34.4 cm^3·K·mol^{-1} is reached at 10 K. Below 10 K, there is an abrupt decrease in the $\chi_M T$ value until a value of 11.2 cm^3·K·mol^{-1} is reached at 1.8 K. For **1**,**2**, and **3** the $\chi_M T$ value at 300 K is less than the calculated spin-only value of 44.2 cm^3·K·mol^{-1} for a molecule comprised of six Mn(II) and six Mn(III) non-interacting ions.

It was also observed from DC magnetic susceptibility measurements that **1**, **2**, and **3** exhibit a field dependence of $\chi_M T$ at low temperatures. The DC magnetic susceptibility data for **1**, **2**, and **3** were collected at fields of 0.1 and 0.01 T, in addition to the 1 T data, and are shown in Figures 5, 6, and 7, respectively. The data for all three complexes show a field dependence below 15 K. As described above, the 1 T data for all three complexes show a decrease in the $\chi_M T$ value at low temperatures. The data for **1** and **3** collected at fields lower than 1 T show an increase in the $\chi_M T$ value at temperatures below 15 K. For the data collected at 0.1 and 0.01 T for **2**, the $\chi_M T$ value continues to decrease as the temperature is decreased from 300 to 10 K, where there is a plateau in the value of $\chi_M T$.

Heat Capacity Measurements. In order to determine the origin of the field dependence observed for these complexes,

(33) Foguet-Albiol, D.; O'Brien, T. A.; Wernsdorfer, W.; Moulton, B.; Zaworotko, M. J.; Abboud, K. A.; Christou, G. *Angew. Chem., Int. Ed.* **2005**, *44*, 897.

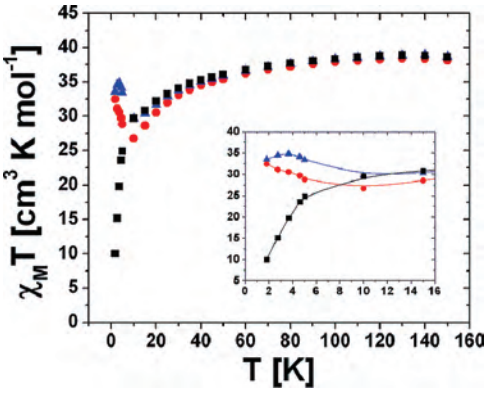

Figure 7. Field dependence for $[Mn_{12}(Edea)_8(CH_3COO)_2(CH_3CH_2COO)_{12}]$ (**3**). Data were collected at 1 (■), 0.1 (▲), and 0.01 T (●) in the temperature range of 1.8−300 K.

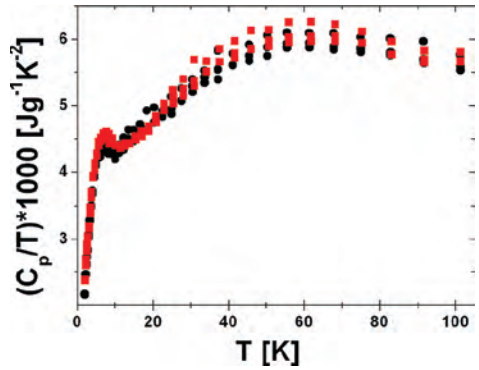

Figure 8. Heat capacity data for $[Mn_{12}(Adea)_8(CH_3COO)_{14}]\cdot 7CH_3CN$ ($\mathbf{1}\cdot 7CH_3CN$). Zero-field cooled data were collected at (●) 0 and (■) 1 T.

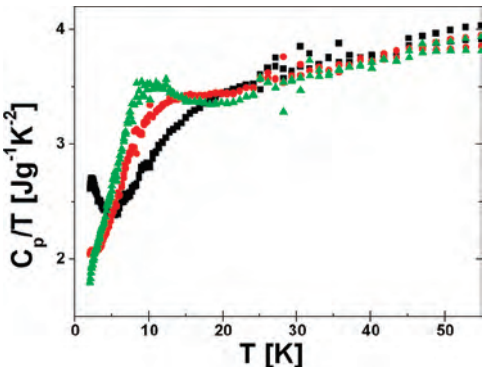

Figure 9. Heat capacity data for $[Mn_{12}(Adea)_8(CH_3COO)_{14}]\cdot 7CH_3CN$ ($\mathbf{1}\cdot 7CH_3CN$) collected at 3 (▲), 5 (●), and 9 T (■).

detailed heat capacity measurements were carried out on polycrystalline samples of **1** and **3**. Heat capacity data were collected in the temperature range of 1.8−100 K and in applied magnetic fields ranging from 0 to 9 T.

A broad peak is seen in the heat capacity measurements for complex **1** at approximately 10 K in the data collected at 0 T (see Figure 8). This peak starts to gradually diminish as stronger magnetic fields are applied, and eventually, at the high fields of 7−9 T, the broad peak at 10 K disappears and is replaced by another broad peak at approximately 2.5 K (see Figure 9). The heat capacity data for complex **3** (Figures 10 and 11) also show a broad feature at 10 K;, however, the increase in magnetic field up to 9 T does not seem to have as dramatic of an effect as in complex **1**.

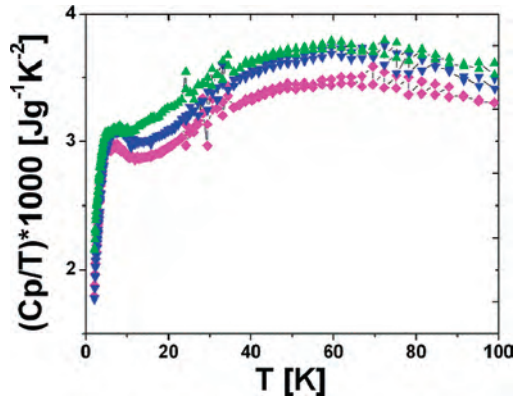

Figure 10. Heat capacity data for $[Mn_{12}(Edea)_8(CH_3COO)_2(CH_3CH_2COO)_{12}]$ (**3**). Field-cooled data collected at 0 (◆), 3 (▼), and 5 T (▲).

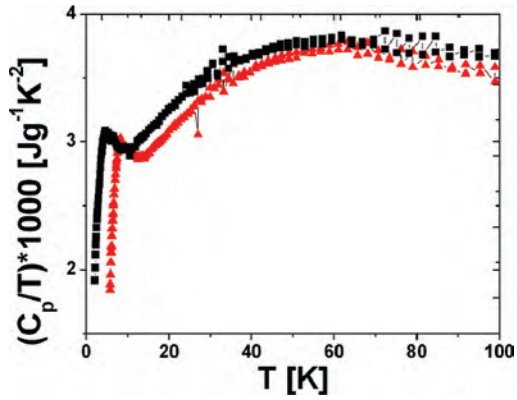

Figure 11. Heat capacity data for $[Mn_{12}(Edea)_8(CH_3COO)_2(CH_3CH_2COO)_{12}]$ (**3**). Field-cooled data collected at 7 (▲) and 9 T (■).

A broad peak in the heat capacity measurements is also seen for other SMMs.[34,35] The $[Mn_4]$ dicubane complexes with $S = 9$ spin ground states, reported by Yoo et al.,[36,37] also show broad peaks in the heat capacity measurements at approximately 7.6 and 5 K at 0 T, which were shifted to lower temperatures as the strength of the applied magnetic field was increased. Since there is no sharp peak corresponding to long-range magnetic ordering observed in the heat capacity data for these $[Mn_4]$ complexes, it was concluded that there is no long-range magnetic ordering in these $[Mn_4]$ complexes.[35]

Complexes **1** and **3** both show a broad peak in their heat capacity data, similar to that observed for the complexes described above. Such a broad peak is usually attributed to the Schottky heat capacity due to the changes in thermal populations in the ground and low-lying excited states. In the presence of large magnetic fields of 7−9 T, the profile of the Schottky effect can change due to Zeeman interactions that are different for different states. If a phase transition

(34) Miyazaki, Y.; Bhattacharjee, A.; Nakano, M.; Saito, K.; Aubin, S. M. J.; Eppley, H. J.; Christou, G.; Hendrickson, D. N.; Sorai, M. *Inorg. Chem.* **2001**, *40*, 6632.
(35) Bhattacharjee, A.; Miyazaki, Y.; Nakano, M.; Yoo, J.; Christou, G.; Hendrickson, D. N.; Sorai, M. *Polyhedron* **2001**, *20*, 1607.
(36) Yoo, J.; Yamaguchi, A.; Nakano, M.; Krzystek, J.; Strieb, W. E.; Brunel, L.-C.; Ishimoto, H.; Christou, G.; Hendrickson, D. N. *Inorg. Chem.* **2001**, *40*, 4604.
(37) Yoo, J.; Brechin, E. K.; Yamaguchi, A.; Nakano, M.; Huffman, J. C.; Maniero, A. L.; Brunel, L.-C.; Awaga, K.; Ishimoto, H.; Christou, G.; Hendrickson, D. N. *Inorg. Chem.* **2000**, *39*, 3615.

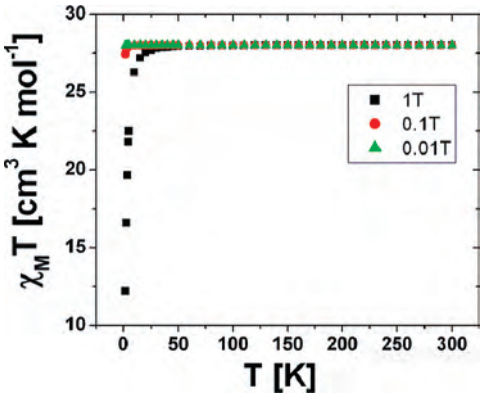

Figure 12. Field dependence plot for a system with an $S = 7$ ground state for fields of 1, 0.1, and 0.01 T.

were occurring in either of these complexes, a sharp peak would be observed in a zero applied magnetic field. Since this is not the case for either **1** or **3**, we can rule out the presence of a phase transition.

There is most likely a simple explanation of the field dependence of $\chi_M T$ vs T data for complexes **1**−**3**. Figure 12 shows a plot of the field dependence calculated for a complex with an $S = 7$ ground state at fields of 0.01, 0.1, and 1 T (assuming there are no low-lying excited states). The $\chi_M T$ values were calculated for the temperature range 300−1.8 K using the equation $M = NgS\mu_B B_j(x)$, where M is the molar magnetic susceptibility, N is Avogadro's number, μ_B is the Bohr magneton, and $B_j(x)$ is the Brillouin function. From this calculation, it was determined that for a system with an $S = 7$ ground state, the spin-only value of $\chi_M T$ at 300 K in a 1 T field is 28 cm^3·K·mol^{-1}. This value remains constant until a temperature of approximately 27 K, below which there is an abrupt decrease in the $\chi_M T$ value until a value of 12 cm^3·K·mol^{-1} is reached at 1.8 K. For fields of 0.1 and 0.01 T, there is no abrupt decrease in the $\chi_M T$ value at low temperatures. These calculations are in agreement with the experimental data collected on complexes **1**, **2**, and **3**. In all three complexes, the 1 T data show an abrupt decrease in the $\chi_M T$ value at low temperatures due simply to the Zeeman interactions. Such an abrupt decrease in the $\chi_M T$ value is not observed in the experimental data for the 0.1 and 0.01 T data for **1**, **2**, or **3** since the Zeeman interactions at these fields are very small.

Field Dependence of DC Magnetic Susceptibility. In order to determine the spin ground state of the complexes, variable-field DC magnetization data were collected at fields from 0.1 to 5 T in a temperature range of 1.8−10 K. In all cases, it was assumed that only one spin state is thermally populated and that the spin Hamiltonian given in eq 1 is appropriate,

$$\hat{H} = D\hat{S}_z^2 + E(\hat{S}_x^2 - \hat{S}_y^2) + g\mu_B \hat{S}\cdot\hat{\mathbf{B}} \qquad (1)$$

where D is the axial zero-field splitting (ZFS) parameter, E is the rhombic ZFS parameter, and **B** is the applied field. Theoretical magnetization values were calculated by using a full-matrix diagonalization approach, and the magnetization of a molecule was evaluated with eq 2. The parameters such as g, D, and E varied, and the best parameters were evaluated in a least-squares fit.

$$M = N\sum_i(\delta E_i/\delta H)\exp(-E_i/kT)/\sum_i \exp(-E_i/kT) \qquad (2)$$

The reduced magnetization data for **1**, **2**, and **3** show that the individual isofields do not superimpose, indicating the presence of a nonzero D value for all three complexes. Two sets of data were collected for all three complexes in order to determine the spin of the ground state. The first set of data was collected at higher fields in the 2−5 T range and at temperatures ranging from 1.8 to 4 K. The second set of data was collected at lower fields from 0.1 to 1 T and in the temperature range of 1.8−10 K. This approach is used due to the presence of low-energy excited states with different spins. The low-field fit tends to give a smaller spin value S for the ground state than does fitting the high-field data.

For complex **1**, the high- and low-field reduced magnetization fits are shown in Figure 13. For **1**, the high-field reduced magnetization data (2−5 T) were fit with the parameters $S = 9$, $g = 1.9$, and $D = -0.33$ cm^{-1}. The data collected at lower fields of 0.1−1 T gave the parameters $S = 9$, $g = 2$, and $D = -0.23$ cm^{-1}. For complex **2**, the high- and low-field reduced magnetization fits are shown in Figure 14. For **2**, data collected at high fields were fit with the parameters $S = 9$, $g = 1.9$, and $D = -0.31$ cm^{-1}. Low-field data for **2** were collected at fields ranging from 0.1 to 2 T and were fit with the parameters $S = 7$, $g = 1.8$, and $D = -0.22$ cm^{-1}. It is clear for complex **2** that the fit of the low-field data is better than that for the high-field data. The high- and low-field reduced magnetization fits are shown in Figure 15 for complex **3**. For **3**, the high-field reduced magnetization data were fit with the parameters $S = 10$, $g = 1.9$, and $D =$

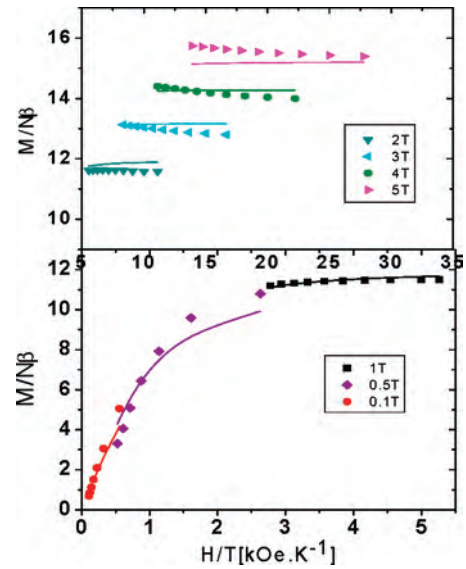

Figure 13. Reduced magnetization ($M/(N\mu_B)$) versus **H**/T, where M is the molar magnetization, N is Avogadro's number and μ_B is the Bohr magneton, **H** is the applied magnetic field in kOe, and T is the temperature in kelvin, for $[Mn_{12}(Adea)_8(CH_3COO)_{14}]\cdot 7CH_3CN$ (**1**·7CH_3CN). The top plot shows data collected at 5, 4, 3, and 2 T in the temperature range of 1.8−3.6 K. Solid lines represent the fit with the parameters $S = 9$, $g = 1.9$, and $D = -0.33$ cm^{-1}. The bottom plot shows data collected at 1, 0.5, and 0.1 T in the temperature range 1.8−10 K. Solid lines represent the fits with the parameters $S = 9$, $g = 2$, and $D = -0.23$ cm^{-1}.

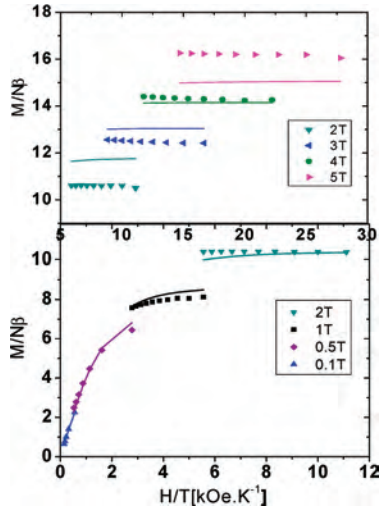

Figure 14. Reduced magnetization for $[Mn_{12}(Edea)_8(CH_3CH_2COO)_{14}]$ (**2**). The top plot shows data collected at 5, 4, 3, and 2 T in the temperature range 1.8−3.4 K. Solid lines represent the fits with the parameters $S = 9$, $g = 1.9$, and $D = -0.31$ cm^{-1}. The bottom plot shows data collected at fields of 0.1, 0.5, 1, and 2 T in the temperature range of 1.8−10 K. Solid lines represent the fits with the parameters $S = 7$, $g = 1.8$, and $D = -0.22$ cm^{-1}.

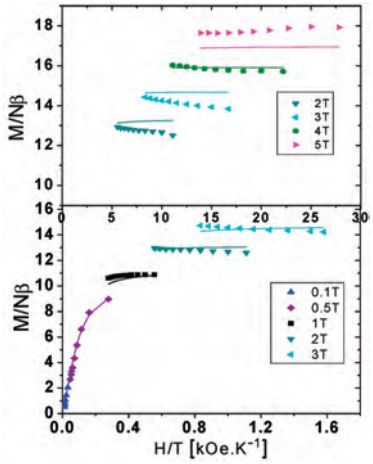

Figure 15. Reduced magnetization for $[Mn_{12}(Edea)_8(CH_3COO)_2(CH_3CH_2COO)_{12}]$ (**3**). The top plot shows data collected at 5, 4, 3, and 2 T in the temperature range of 1.8−3.6 K. Solid lines represent the fit with the parameters $S = 10$, $g = 1.9$, and $D = -0.29$ cm^{-1}. The bottom plot shows data collected at fields of 0.1, 0.5, 1, 2, and 3 T in the temperature range of 1.8−10 K. Solid lines represent the fits with the parameters $S = 9$, $g = 1.8$, and $D = -0.17$ cm^{-1}.

−0.29 cm^{-1}. The low-field data for **3** were collected at fields ranging from 0.1 to 3 T and were fit with the parameters $S = 9$, $g = 1.8$, and $D = -0.17$ cm^{-1}. Again, for complex **3**, the low-field fit seems more reliable than the high-field fit.

AC Magnetic Susceptibility Studies. AC magnetic susceptibility data were collected on complexes **1**, **2**, and **3** in a zero applied DC field with an oscillating AC field of 3 Oe as shown in Figures 16, 17, and 18, respectively. The top portions of these figures show plots of the product of in-phase AC susceptibility and absolute temperature ($\chi_M'T$) vs temperature, while the bottom portions show the plots of the out-of-phase AC susceptibility (χ_M'') vs temperature. Data were collected at temperatures ranging from 1.8 to 4.6 K and at six different frequencies of 50, 99, 250, 498, 801, and 997 Hz.

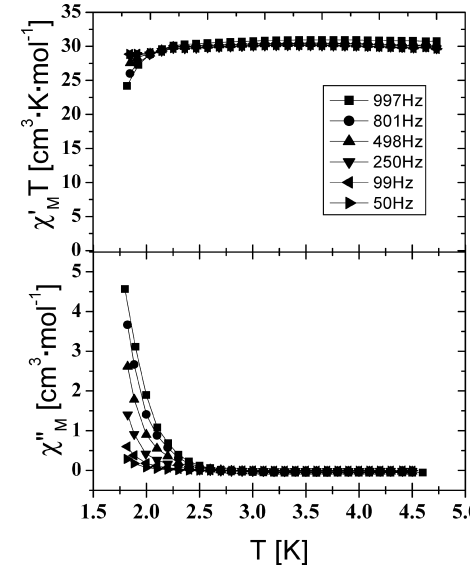

Figure 16. AC susceptibility data for $[Mn_{12}(Adea)_8(CH_3COO)_{14}]\cdot 7CH_3CN$ (**1**·7CH$_3$CN). Data were collected with an oscillating magnetic field of 3 Oe.

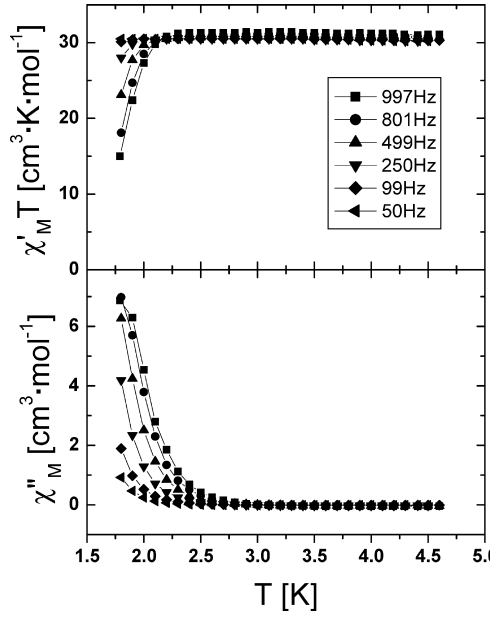

Figure 17. AC susceptibility data for $[Mn_{12}(Edea)_8(CH_3CH_2COO)_{14}]$ (**2**). Data were collected in an oscillating magnetic field of 3 Oe.

For complexes **1**, **2**, and **3**, the in-phase AC susceptibility data collected at 50 Hz were least-squares fit and then extrapolated to 0 K to estimate the ground-state spins of the three complexes. The extrapolated AC data for **1**, **2**, and **3** are shown in Figure 19. Two separate extrapolations were carried out on the data for **1**. In the first case, data taken from 1.8 to 3.0 K were extrapolated to 0 K to give a value of $\chi'_M T = 25.9$ cm^3·K·mol^{-1}. In the other case, the AC data for **1** collected from 3.1 to 4.5 K were extrapolated to 0 K, giving a value of $\chi'_M T = 29.8$ cm^3·K·mol^{-1}. Both extrapolations for complex **1** support an $S = 7$ ground state predicted by the spin-only formula and further substantiated by the hysteresis data given in the next section.

For complex **2**, extrapolation of the in-phase data collected at 50 Hz gives a value of 30.8 cm^3·K·mol^{-1}, which also

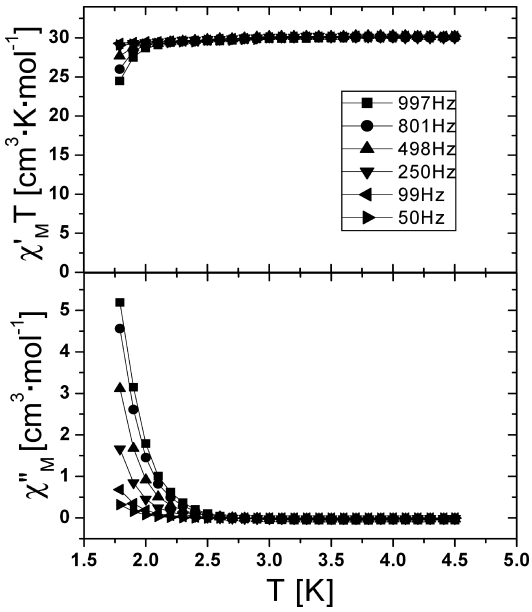

Figure 18. AC susceptibility data for $[Mn_{12}(Edea)_8(CH_3COO)_2(CH_3CH_2COO)_{12}]$ (**3**). Data were collected in a 3 Oe oscillating magnetic field.

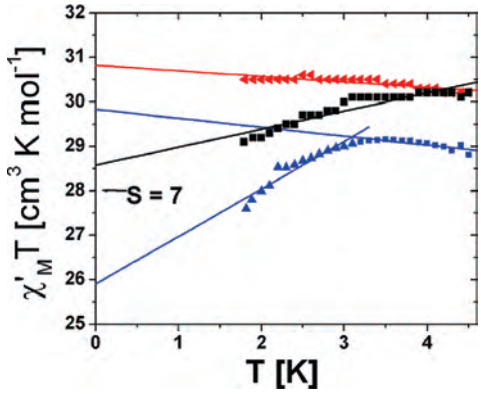

Figure 19. Extrapolation of 50 Hz in-phase AC susceptibility data for complexes for $[Mn_{12}(Adea)_8(CH_3COO)_{14}]\cdot 7CH_3CN$ (**1**·7CH_3CN) (blue triangles), $[Mn_{12}(Edea)_8(CH_3CH_2COO)_{14}]$ (**2**) (red triangles), and $[Mn_{12}(Edea)_8(CH_3COO)_2(CH_3CH_2COO)_{12}]$ (**3**) (black squares). Data were collected in a 3 Oe oscillating magnetic field and were extrapolated to 0 K.

corresponds to an $S = 7$ ground state according to the values obtained from the spin-only formula. A similar result for **3** was found in the extrapolation, giving a value of 28.6 $cm^3\cdot K\cdot mol^{-1}$, which corresponds to an $S = 7$ ground state.

Complexes **1**, **2**, and **3** show frequency-dependent out-of-phase signals in the AC susceptibility measurements indicating slow magnetization relaxation relative to the frequency of the oscillating AC field at low temperatures. A full peak in the out-of-phase signal cannot be seen in the temperature range in which the measurements were carried out. The presence of a frequency-dependent out-of-phase signal in the AC susceptibility measurements indicates that **1**, **2**, and **3** are likely SMMs.

Magnetization Hysteresis Studies. Magnetization hysteresis measurements were carried out on all three $[Mn_{12}]$ wheel complexes by the use of a high-sensitivity micro-Hall effect magnetometer at temperatures down to 0.1 K. Information such as the spin ground states of the $[Mn_{12}]$

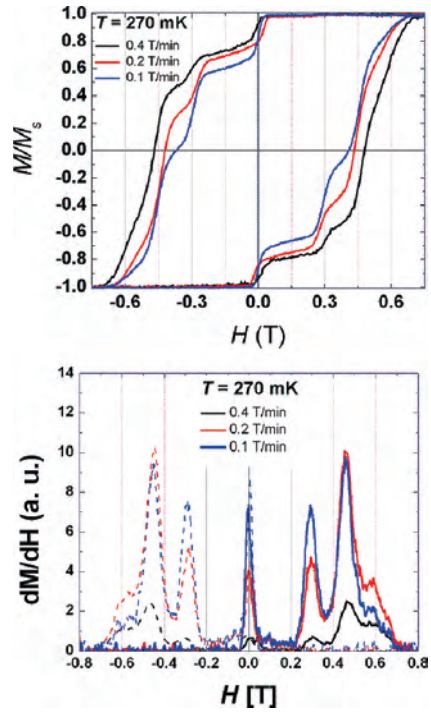

Figure 20. The top panel shows a single-crystal magnetization hysteresis loop for $[Mn_{12}(Adea)_8(CH_3COO)_{14}]\cdot 7CH_3CN$ (**1**·7CH_3CN) collected at 0.27 K at different sweep rates of 0.1, 0.2, and 0.4 T/min, and the bottom panel shows the first derivative (d*M*/d**H**) plotted versus field **H**.

wheels, the blocking and crossover temperatures of the complexes, and the anisotropy parameters of their magnetic Hamiltonian was obtained from the hysteresis measurements.

Magnetization hysteresis measurements were carried out on a single crystal of $[Mn_{12}(Adea)_8(CH_3COO)_{14}]\cdot 7CH_3CN$ (**1**·7CH_3CN) and in the temperature range of 0.27−0.9 K. The hysteresis loops shown in Figure 20 were collected at a constant temperature of 0.27 K and at different sweep rates of 0.4, 0.2, and 0.1 T/min. Steps are observed at regular intervals in the hysteresis loop and are attributed to QTM.[2] The bottom portion of Figure 20 shows the first derivative of magnetization (d*M*/d**H**) plotted versus the field **H**. The peaks seen in the bottom portion of Figure 20 correspond to the fields at which steps due to resonant QTM are observed in the hysteresis data. Four peaks are observed at 0, 0.29, 0.45, and 0.58 T.

The crossover temperature was determined to be approximately 0.3 K, below which tunneling occurs exclusively through the ground states. This was determined from the coercive field behavior plotted versus temperature as shown in Figure 21, from which the blocking temperature (T_B = 0.85 K) was also extracted. The superparamagnetic magnetization curve at 0.9 K ($>T_B$) was fit to a hyperbolic tangent and indicates an $S = 7$ ground state with $g = 2$ and $D = -0.405$ K.

Resonances at 0, 0.29, and 0.58 T can be explained in terms of resonant QTM between opposite projections of a simple spin $S = 7$ along the easy magnetic axis of the molecule (using the parameters given above and $H_k = k \times 0.29$ T, with $k = 0$, 1, and 2). However, there are two extra resonances observed in the hysteresis measurements: one at

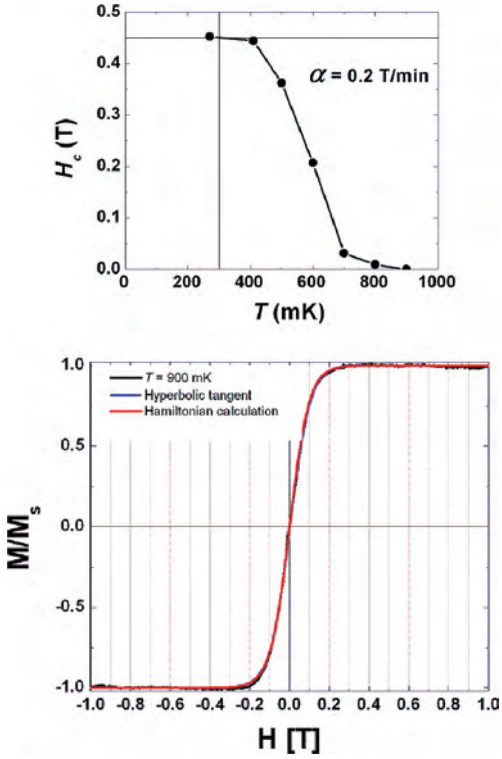

Figure 21. Coercive field behavior for $[Mn_{12}(Adea)_8(CH_3COO)_{14}]\cdot 7CH_3CN$ (**1**·$7CH_3CN$). The top portion shows a plot of the coercive field versus temperature. The bottom portion shows magnetization curve at 0.9 K fit to a hyperbolic tangent.

0.15 T, which is only observed over 0.5 K (not shown here), and the other at 0.45 T observed at low temperatures. The observation of these two resonances is a manifestation of the dimeric magnetic structure of this molecule as a result of a weaker exchange coupling between the Mn5 and Mn6 ions at opposite sites of the wheel, which are separated by a larger distance ($d_{56} \approx 3.489$ Å) than the rest of the Mn ions ($d_{avg} = 3.173$ Å). Consequently, the molecule behaves as a dimer of two ferromagnetically exchange-coupled $S = {}^7/_2$ halves giving rise to both $S = 7$ and $S = 6$ entangled spin states at low temperature whose anticrossings with magnetic field generate the observed extra resonances.[38,39]

Hysteresis measurements were also carried out on a single crystal of $[Mn_{12}(Edea)_8(CH_3CH_2COO)_{14}]$ (**2**). Hysteresis data were collected at temperatures ranging from 0.1 to 0.9 K. Figure 22 shows the hysteresis data collected at a sweep rate of 0.1 T/min and at temperatures ranging from 0.1 to 0.9 K. Steps due to QTM are clearly observed. The crossover and blocking temperatures were determined to be 0.35 and 0.8 K, respectively. Figure 23 shows the dependence of the d*M*/d**H** peaks (i.e., QTM resonances) on the angle of application of the magnetic field with respect to one of the crystallographic axes of the sample. Different peaks follow different behaviors with field, indicative of the presence of two molecular orientations within the crystal, as seen in the crystal structure of **2**. The lines of different color in Figure

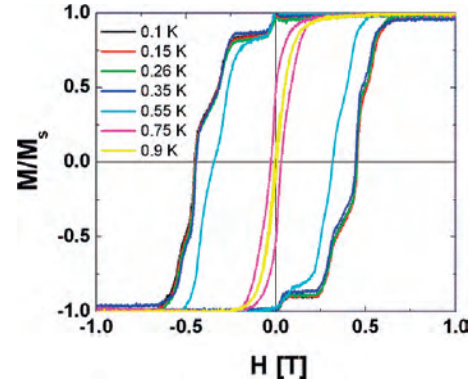

Figure 22. Magnetization hysteresis plot for $[Mn_{12}(Edea)_8(CH_3CH_2COO)_{14}]$ (**2**). Data were collected at temperatures ranging from 0.1 to 0.9 K and at a sweep rate of 0.1 T/min.

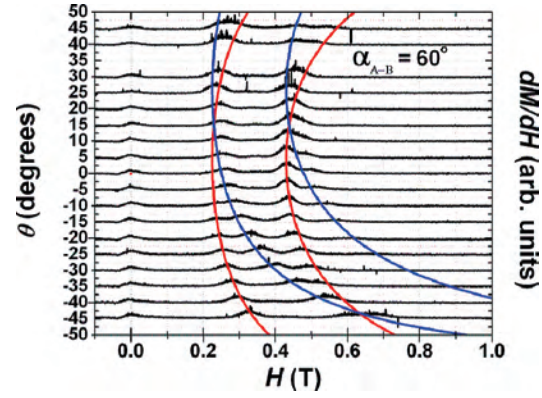

Figure 23. Magnetization dependence on the angle of the application of the magnetic field for $[Mn_{12}(Edea)_8(CH_3CH_2COO)_{14}]$ (**2**).

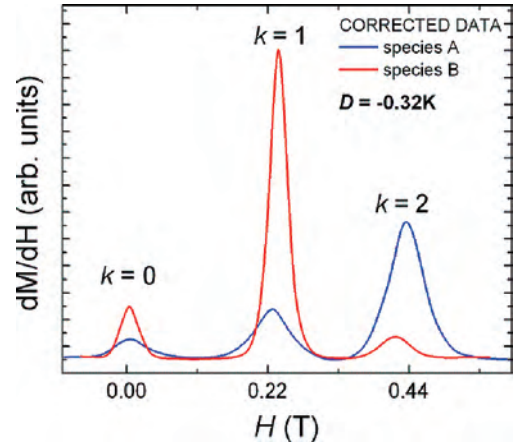

Figure 24. First derivative of magnetization (d*M*/d**H**) versus DC field for $[Mn_{12}(Edea)_8(CH_3CH_2COO)_{14}]$ (**2**). The *D* value was estimated to be −0.3 K from the spacing of the resonances.

23 are fits of the data using an angle of 50° between the easy axes of both species, in excellent agreement with the molecular orientations obtained from the crystal structure. The data corresponding to the two species were corrected and plotted separately in Figure 24, in which three QTM resonances, $H_k = k \times 0.22$ T (with $k = 0$, 1, and 2) are clearly observed for both species. The results indicate an $S = 7$ ground state with axial zero-field splitting parameter $D = -0.32$ K calculated from the spacing between resonances.

(38) Ramsey, C. M.; Del Barco, E.; Hill, S.; Shah, S. J.; Beedle, C. C.; Hendrickson, D. N. *Nat. Phys.* **2008**, *4*, 277.
(39) Cano, J.; Costa, R.; Alvarez, S.; Ruiz, E. *J. Chem. Theory Comput.* **2007**, *3*, 782.

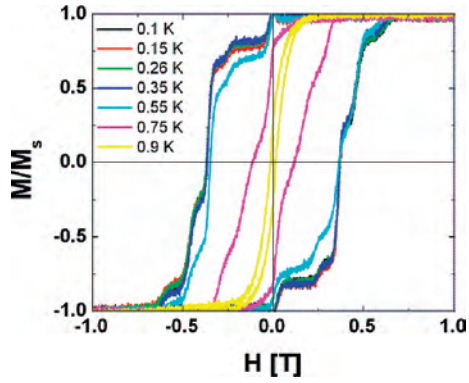

Figure 25. Magnetization hysteresis loop for $[Mn_{12}(Edea)_8(CH_3COO)_2(CH_3CH_2COO)_{12}]$ (**3**). Data were collected at temperatures ranging from 0.1 to 0.9 K and at a sweep rate of 0.1 T/min.

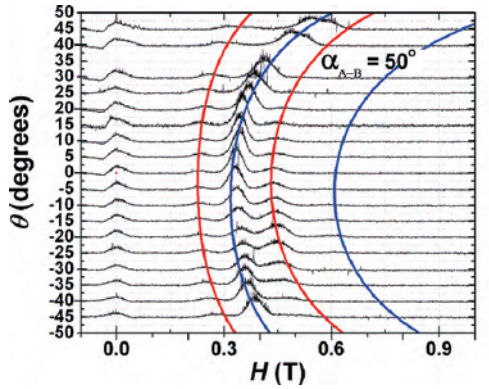

Figure 26. Magnetization dependence on the angle of the application of the magnetic field for $[Mn_{12}(Edea)_8(CH_3COO)_2(CH_3CH_2COO)_{12}]$ (**3**).

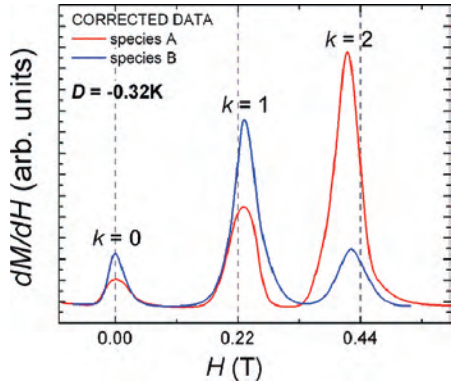

Figure 27. First derivative of magnetization (d*M*/d**H**) versus DC field for $[Mn_{12}(Edea)_8(CH_3COO)_2(CH_3CH_2COO)_{12}]$ (**3**).

Hysteresis measurements were also carried out on a single crystal of $[Mn_{12}(Edea)_8(CH_3COO)_2(CH_3CH_2COO)_{12}]$ (**3**). Figure 25 shows the hysteresis data collected at a sweep rate of 0.1 T/min and at temperatures ranging from 0.1 to 0.9 K, from which the blocking and crossover temperatures were determined to be 0.8 and 0.35 K, respectively. Figure 26 shows the angle dependence of the magnetization derivatives versus magnetic field, following the same procedure as in the case of complex **2**, *vide supra*. As in complex **2**, the data show the presence of two distinct molecular orientations within the unit cell. The corrected d*M*/d**H** versus **H** curves shown in Figure 27 were obtained using the fitting parameters of the data in Figure 26 with an angle of 60° between the easy axes of each molecular species, also in excellent agreement with the molecular orientations determined from the crystal structure. The results for complex **3** indicate an $S = 7$ ground state with axial zero-field splitting parameter $D = -0.32$ K.

Interestingly, neither complex **2** nor **3** shows extra QTM resonances, as seen in complex **1**. This indicates that the wheels in **2** and **3** behave as simple $S = 7$ systems at low temperature. This can be easily understood looking at the relative values of d_{16} or d_{56} (distance between Mn1 and Mn6′ ions in **2** and **3** or between Mn5 and Mn6 in **1**, respectively) compared to d_{avg} (average distance between the rest of Mn ions in each wheel) for all three complexes. While d_{16} (d_{56} in **1**) is similar among the three (3.489, 3.496, and 3.488 Å in **1**, **2**, and **3**, respectively), and one could expect the exchange interaction between these two ions to be similar for all wheels, d_{avg} is shorter in **1** (3.173 Å) compared with those in **2** and **3** (3.1988 and 3.956 Å, respectively). This can be better seen by looking at the ratio between both distances, d_{56}/d_{avg} for **1** or d_{16}/d_{avg} for **2** and **3**, which is largest in complex **1** at 1.0995. Note that it is the relative value between the interatomic distances that determines the magnetic rigidity of the wheel.

In the case of complex **1**, the difference between these distances is enough to make it behave as two rigid halves ($S = {}^7/_2$) weakly coupled ferromagnetically by exchange interactions. In complexes **2** and **3**, the difference is not sufficient enough to break the wheel into two magnetic entities, and the molecule behaves as a simple $S = 7$ wheel at low temperature. Interestingly, the small variation of d_{avg} (~0.02 Å) has a substantial effect on the exchange parameters within the wheel and the overall magnetic properties (i.e., distance variations of 0.2 Å generate changes of more than 2 orders of magnitude in the exchange coupling within the wheel).[33]

Summary and Conclusions

The structures and magnetic properties are reported for three new $[Mn_{12}]$ wheel-shaped complexes: $[Mn_{12}(Adea)_8(CH_3COO)_{14}]\cdot 7CH_3CN$(**1**$\cdot 7CH_3CN$),$[Mn_{12}(Edea)_8(CH_3CH_2COO)_{14}]$ (**2**), and $[Mn_{12}(Edea)_8(CH_3COO)_2(CH_3CH_2COO)_{12}]$ (**3**). In comparison to the three $[Mn_{12}]$ wheels reported[25] previously, these complexes were prepared with either more shielding carboxylate substituents or *N*-alkyl diethanolamine ligands. Complexes **2** and **3** also do not cocrystallize with solvent molecules, which minimizes the number of microenvironments. This can lead to magnetization hysteresis with better resolved "steps" associated with the quantum tunneling of the direction of magnetization.

All three of these new $[Mn_{12}]$ wheel complexes were shown to have $S = 7$ ground states with low-lying excited spin states. Single crystals of all three complexes exhibit hysteresis in their magnetization vs magnetic field plots. Thus, all three complexes are SMMs, as also indicated by the presence of frequency-dependent out-of-phase AC susceptibility signals.

A detailed study of the magnetization vs magnetic field responses shows that all three complexes exhibit the normal $k = 0$, 1, and 2 resonances ("steps") in their magnetization

hysteresis plots. It was interesting to find that complex **1** also exhibits extra resonances that can be explained[38] by the presence of a low-lying $S = 6$ excited state. It has been shown[38] that there is quantum interference of tunnel trajectories between states of different spin.

Acknowledgment. This work was supported by the National Science Foundation (NSF).

Supporting Information Available: Figures detailing heat capacity measurements and crystallographic information. This material is available free of charge via the Internet at http://pubs.acs.org. CCDC 695723, 695724, and 695725 contain the supplementary crystallographic data for complexes **1**, **2**, and **3**, respectively. These data can be obtained free of charge from The Cambridge Crystallographic Data Centre via www.ccdc.cam.ac.uk/data_request/cif.

IC801374U